Modelling melt pool dynamics in aluminium-to-steel welds performed by Friction Melt Bonding: a challenge addressed with the Particle Finite Element Method

Eduardo Fernández[1*], Martin Lacroix[1], Simon Février[1], Tianyu Zhang[1], Luc Papeleux[1], Billy-Joe Bobach[1], Romain Boman[1], Sophie Ryelandt[2], Aude Simar[2], Jean-Philippe Ponthot[1]

[1*]Aerospace and Mechanical Engineering, University of Liege, Belgium.
[2]Institute of Mechanics, Materials and Civil Engineering, Université Catholique de Louvain (UCLouvain), Louvain-la-Neuve, Belgium.

*Corresponding author(s). E-mail(s): efsanchez@uliege.be;

Abstract

Friction Melt Bonding (FMB) allows to weld aluminium and steel plates in a lap-joint configuration. FMB produces a melt pool in the aluminium plate, which is visually inaccessible as it is trapped between the two plates. As the melt pool boundaries are initially unknown and evolve during the process, numerical simulation is essential to support quantitative research on the FMB process or to predict behaviour in out-of-laboratory conditions. To simulate the FMB process, this work proposes a partitioned methodology that combines PFEM (Particle Finite Element Method) and FEM. PFEM is used for modelling the aluminium plate, including phase change and convective flow within the melt pool. FEM, on the other hand, is used for the steel plate and the accompanying equipment, as they do not present complex multiphysics phenomena such as phase change and evolving boundaries. A 2D model was used for the experimental comparison, as numerous simulations were required to set up the thermal model. Results were compared against experimental measurements. A good agreement between numerical and experimental results was achieved, both for the melt pool geometry and the temperature of a thermocouple. In addition, the effect of ignoring the convective flow inside the melt pool was also studied. In this regard, results show moderate differences in melt pool geometries between flowing and a non-flowing melt pool models.

Keywords: welding simulation, dissimilar metal welding, melt pool, FMB, PFEM

1 Introduction

High performance engineering designs often entail multiple materials. This introduces manufacturing challenges, especially in designs composed of dissimilar metals and when welding is the only joining mechanism tolerated by mechanical or design conditions [1]. In this context, a promising process for welding aluminium and steel plates in lap-joint configuration is the Friction Melt Bonding (FMB) process [2]. In FMB, a cylindrical non-consumable rotating tool is pressed against a steel plate with a force f_{tool}, generating heat by friction, as illustrated in Fig. 1. Under the steel plate is the aluminium plate, and under this a
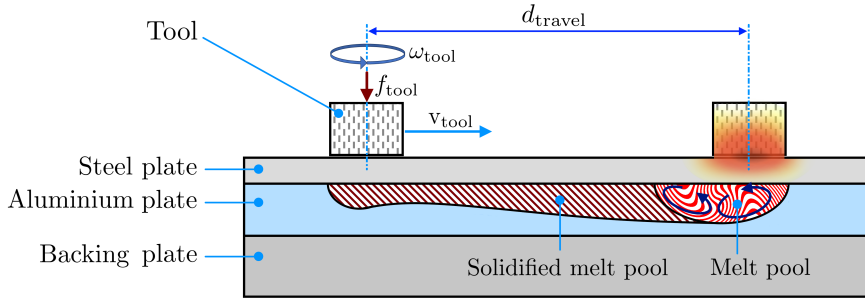
Fig. 1 Illustration of the FMB (Friction Melt Bonding) process for lap-joint welding of steel and aluminium plates. The generated heat raises the temperature of the aluminium plate beyond the melting point, creating a melt pool shown as curved red lines. Inside, liquid aluminium flows redistributing the heat. The rotating tool is displaced a distance d_{travel} in the illustration, leaving a trace of the melt pool (hatched zone in dark red).

thicker plate that serves as mechanical support and heat sink. The generated heat is transmitted to the aluminium plate by conduction, and if accurately controlled, will partially melt the aluminium plate forming a melt pool of liquid metal. Given that the melt pool touches the bottom surface of the steel plate, welding by interdiffusion is achieved between the dissimilar plates. If necessary, the tool can be displaced a distance d_{travel} at some speed v_{tool} to generate a weld bead between the steel and aluminium plates, as illustrated in Fig. 1.

The mechanical conditions imposed on the tool depend on the required heat to melt the aluminium plate. The thicker the steel plate, the greater the dissipated heat, and thus higher loads have to be applied to the tool to reach the melting temperature in the aluminium plate. Due to the service life of the tool, the process is particularly efficient for small thickness of steel plate (approximately 1.0 mm). For this reason, the FMB process could find use in shielding applications in the automotive industry or in storage tanks [1, 3]. In such cases, the aluminium plate may also be thin, imposing a challenge to the FMB process: to generate enough heat to melt the aluminium plate, but not too much in order to avoid melting the full thickness of the plate and thus to avoid melting or damaging the steel and backing plates. However, the heat transmitted to the aluminium plate depends on multiple factors, such as the rotational speed of the tool (ω_{tool}), the travel speed (v_{tool}), the applied force (f_{tool}), the tool dwell time (the time the tool remains in the same position but in contact with the plate), the thickness of the plates, the force applied to hold the plates together, and

the convection and radiation losses between the plates and the environment. In addition, the heat flux and pressure at the welding interface have an impact on the presence of fragile intermetallic compounds, hot tearing, and residual stresses, i.e. aspects defining the quality of the welded joint [4].

Based on the above, a successful aluminium-to-steel weld depends on numerous factors and may be subject to tight FMB operating ranges. Determining the set of parameters and conditions that result in a successful weld joint can be laborious and highly costly if numerous tests are required to adjust the FMB process to each specific demand. For this reason, numerical simulation becomes essential. Several works can be cited in this context. For example, Crucifix et al. [5] use a purely thermal finite element model to obtain the temperature field in the aluminium plate. The melt pool geometry is identified by an isothermal curve at the melting temperature, while the phase change is represented by the change in the physical properties of the material, such as density, thermal conductivity, and specific heat capacity. The same model was used by Jimenez-Mena et al. [4] to qualitatively study the hot tearing phenomenon in the FMB process. Similar studies have been conducted in [6] for studying the intermetallics formation in the joining of aluminium and copper. In all these works, the latent heat of phase change is accounted for by modifying the specific heat capacity (apparent heat capacity method), while convection effects within the melt pool were not considered. The latter aspect is extremely difficult to incorporate in a thermo-mechanical finite element model, as the melt pool

must be considered as a fluid in order to accurately capture the heat distribution due to convective flow. However, the boundary of the melt pool is transient, making it difficult to combine a solid finite element model with a Computational Fluid Dynamics (CFD) model.

Outside the Friction Melt Bonding framework, there are several works that address the simulation of the Rotary Friction Welding (RFW), which is considered as a solid-state welding process, i.e. without a melt pool. For this reason, thermo-elastic-plastic finite element models have been shown to be quite accurate [7], even in commercial software [8] for dissimilar metals. Another vast number of works are found in the simulation of Friction Stir Welding (FSW), which is also a solid-state joining process [9]. As in RFW, thermo-elasto-plastic finite element models are abundant in the literature, although there are also works that resort to CFD models to understand the influence of the tool geometry on the material flow [9, 10].

The applicability of solid finite element models to simulate welding processes is limited when the influence of the melt pool is not negligible. For this reason, other authors have proposed more advanced models, for example, using particle based methods such as Smoothed Particle Hydrodynamics (SPH) and the Discrete Element Method (DEM) (see [11] for a recent review). The discrete character of particles in a Lagrangian framework eases the capture of geometrical and physical discontinuities of the material, which allows to integrate multiphysics models in a single numerical environment and thus to simulate material transformations. However, the focus of these methods as tools for the simulation of melt pools is being directed towards the Additive Manufacturing (AM) field, such as Powder Bed Fusion and Direct Energy Deposition processes (see [12] for a recent review). In such cases, the melt pool can be several orders of magnitude smaller than in FMB, and be submitted to additional physical phenomena due to the presence of a free surface and the use of a laser or electron beam as a heat source. These aspects inevitably increase the complexity of models and hence the computational time, limiting the applicability of SPH and DEM to models of the order of the AM melt pool size.

In distinction to the literature devoted to the simulation of the FMB process, this work employs a particle-based method to cope with the formation and dynamics of the melt pool present in the aluminium plate. The adopted technique is the Particle Finite Element Method (PFEM) [13]. Unlike SPH and DEM, PFEM solves the governing equations using the Finite Element Method (FEM). For that, a finite element mesh is created using a Delaunay triangulation of the particles and it is reconstructed when particles displacements excessively deform the elements. Given that PFEM is based on FEM, it is possible to reuse many of the developments that have already been successfully validated in the FEM literature. For this reason, since its origins in the fluid mechanics field [13], PFEM has rapidly expanded to cover, for example, the simulation of solids, fluid-structure interactions, and phase changes (see [14] for a recent review).

The potential of PFEM to simulate multiphysics and complex engineering problems is becoming well established in the literature. Engineering applications range from the simulation of landslide [15] to the melting of a nuclear corium core [16]. Thus, the present work also aims to contribute to a new engineering application in which the potential of PFEM stands out. Specifically, the objective of PFEM here is to capture melting and solidification that take place in the aluminum plate of the FMB process, taking into account melt pool dynamics. The PFEM model used in this work was documented and validated in a previous contribution [17], which models the molten pool as a Newtonian fluid, while the mechanical response of the solid phase is omitted. Due to this simplification, the proposed methodology for the simulation of the FMB process is limited to examine the geometry of the melt pool and its evolution. Although these aspects can be also captured by Eulerian-based CFD methods, the envisaged goal of this work is to incorporate constitutive laws in the solid phase to obtain its mechanical response upon solidification [18], which is not straightforward to achieve in a CFD framework though highly feasible in PFEM [18]. Paving the way towards FMB simulation using PFEM, future research will focus on considering other aspects that define the quality of the weld such as the presence of brittle intermetallic compounds, the hot tearing phenomenon, or residual stresses.

3
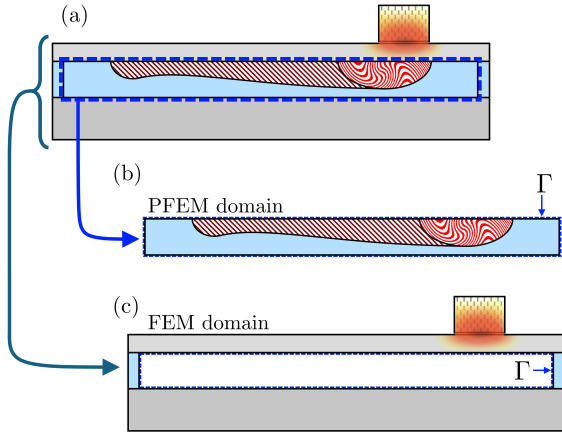
Fig. 2 Illustration of the FMB domain partition used in this work. (a) The complete FMB domain, (b) the PFEM domain and (c) the FEM domain. Γ denotes the common surface between FEM and PFEM domains.

The remainder of the manuscript is organised as follows. Section 2 presents the numerical strategy to simulate the FMB process. Section 3 reports simulation results and provides comparison with experimental results of the FMB process. Finally, section 4 gathers the final conclusions of this work.

2 Numerical model of the Friction Melt Bonding process

As the phase change takes place only in the aluminium plate, it is unpractical to model the whole FMB domain with PFEM. So the FMB process is partitioned into two sub-thermomechanical models (FEM + PFEM), as illustrated in Fig. 2. The PFEM submodel is to simulate phase change (melting and solidification) in the aluminium plate (Fig. 2b). The FEM submodel is used for the parts that remain solid during the FMB process, i.e. the tool, the steel and backing plates, and the extremities of the aluminium plate that are not at risk of being melted (Fig. 2c). This partitioned scheme is widely used in multiphysics simulation, especially for fluid-structure interactions [19, 20], as it allows the use of specialised software for each physics, which are coupled by Dirichlet-Neumann boundary conditions through a third code.

Specifically, the FEM and PFEM models are solved using our own specialised pieces of software. For FEM we use METAFOR [21], which is able to simulate solids subject to large deformations, plasticity and contact. METAFOR has been widely validated for the simulation of metal forming processes but has also been used in other fields, including the simulation of Friction Stir Welding [22]. On the other hand, for PFEM we use a code named PFEM3D [23], which is able to simulate free surface fluid flows, natural convection and phase change [17]. Finally, the METAFOR and PFEM3D software are coupled in a Dirichlet-Neumann scheme using a third code named CUPyDO [24]. The three codes, METAFOR, PFEM3D and CUPyDO, are developed in our computational laboratory. Details on the thermomechanical models used in this work are given in the following subsections.

2.1 Finite element model

Given that the FMB process presents numerous complex physical phenomena, whose models lead to a large number of unknown parameters, simplifications are necessary in order to keep a manageable amount of unknown parameters. However, even with simplifications, it is inevitable to have to solve a large number of problems to find the set of model parameters representative of the FMB process. For this reason, this work is mainly limited to two dimensions (2D), taking into account that our 3D FEM+PFEM model implementation takes 15 times longer to simulate the FMB process than the 2D model. A comparison between 2D and 3D models is given later, in section 3.2.

Having limited the model to 2D, it is no longer feasible to account for the rotation of the tool and the generation of heat by friction. So, the heat transferred to the steel plate must be modelled differently. Among the many ways that can be thought of, in this work we assume that the tool is perfectly rigid and at constant temperature T_{tool}, as shown in Fig. 3. That is, the tool acts as a heat reservoir that transfers heat to the steel plate by contact. The thermal conductance from the tool to the plate is modelled as:

$$h_{\text{tool}} = h_{\text{c0}} \left(\frac{p}{H_{\text{v}}} \right)^w \tag{1}$$
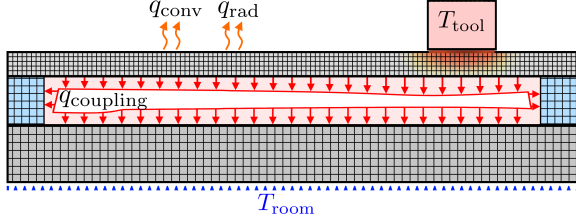
Fig. 3 Thermal boundary conditions of the FEM sub-model.

Fig. 4 Illustration of the displacement imposed on the tool for the simulation of the FMB process.

where h_{c0} is the nominal thermal conductance between the tool and the steel plate, p is the contact pressure, H_v is the Vickers hardness of the steel plate, and w is an experimentally determined exponent [25].

The mechanical contact between the tool and the steel plate is controlled by vertical displacement of the tool as follows. At the beginning of the simulation, the lower face of the rigid tool is placed against the upper face of the steel plate, and over a time span of t_{ph}, a vertical descent of the tool is imposed, as shown in Fig. 4. This procedure corresponds to the preheating phase and the vertical distance travelled by the tool (d_{tool}) is called the (numerical) penetration distance. After the preheating phase, the tool starts its horizontal displacement at velocity v_{tool}.

Regarding the heat transfer between plates, it is considered that the plates are perfectly bonded, so there is no relative displacement between them at the interface and no thermal contact resistance.
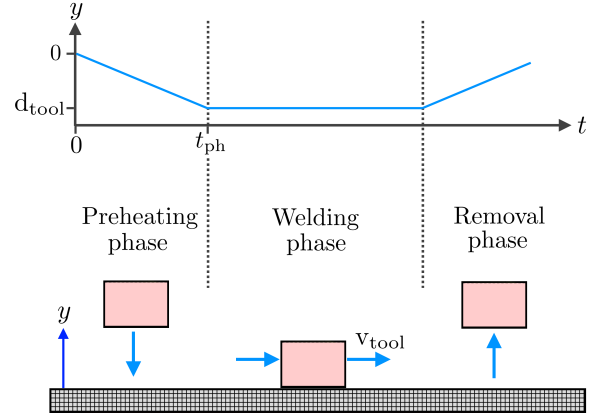
In view of the above, an isotropic thermoelastic model is used as the constitutive model for the FEM parts. The governing equations are the momentum, mass and energy conservation equations, as follows:

$$\rho \, \frac{d^2\mathbf{x}}{dt^2} - \nabla \cdot \boldsymbol{\sigma} = 0 \qquad (2a)$$

$$\rho \, J = \rho_0 \qquad (2b)$$

$$\rho \, c_v \, \frac{dT}{dt} + \nabla \cdot \boldsymbol{q} = 0 \qquad (2c)$$

where ρ is density, $\mathbf{x}$ is the current position vector, d/dt is the Lagrangian time derivative, $\boldsymbol{\sigma}$ is the Cauchy stress tensor defined by an objective thermo-hypo-elastic consitutive law, $\nabla\cdot$ is the divergence operator, J is the determinant of the deformation gradient tensor, ρ_0 is the initial density, c_v is the specific heat capacity, T is temperature, and the last term $\boldsymbol{q}$ is the heat flux vector defined by the Fourier's law as follows:

$$\boldsymbol{q} = -\kappa \nabla T \qquad (3)$$

where κ is the thermal isotropic conductivity and ∇ is the gradient operator. Eq. (2) is complemented with Dirichlet and Neumann boundary conditions. Specifically, a constant temperature equal to the room temperature is imposed at the base of the backing plate, as shown in Fig. 3. In addition, heat flux by convection, radiation and from the tool are considered, which are respectively defined as:

$$\boldsymbol{q}_{conv} = h_{conv}(T - T_{room}) \, \hat{\boldsymbol{n}} \qquad (4a)$$

$$\boldsymbol{q}_{rad} = \epsilon_{rad} \, \sigma_{SB} \, (T^4 - T_{room}^4) \, \hat{\boldsymbol{n}} \qquad (4b)$$

$$\boldsymbol{q}_{tool} = h_{tool}(T - T_{tool}) \, \hat{\boldsymbol{n}} \qquad (4c)$$

where ϵ_{rad} is the material emissivity, σ_{SB} is the Stefan-Boltzmann constant, h_{conv} is the convective heat transfer coefficient, T is the local temperature, T_{room} is the room temperature, and $\hat{\boldsymbol{n}}$ is the surface outward unit normal vector. For coupling with the PFEM submodel, a heat flux $\boldsymbol{q}_{coupling}$ is imposed on the inner surfaces of the FEM submodel, representing the heat exchanged with the PFEM submodel. Regarding the mechanical boundary conditions, the bottom surface is fixed to prevent displacements in all its degrees of freedom. The tool is controlled in position, as explained previously and as illustrated

in Fig. 4. It is important to note that the internal surfaces (that communicate with the PFEM submodel) have also been constrained in displacement because, as discussed in the introduction and explained in the following section, the constitutive model used in the PFEM submodel is oversimplified for the solid phase and prevents the computation of strains and stresses, and thus, the computation of reaction forces.

The weak form of Eq. (2) are discretised using linear quadrilateral elements for the position and temperature field, Generalised-α time integration scheme is used, and the mechanical and thermal parts of the FEM model are solved in a staggered scheme [26, 27]. The contact between the tool and the steel plate is modelled using a node-to-segment scheme [28] and is solved by the penalty method [21].

2.2 Particle Finite Element Model

The aluminium plate portion at risk of being melted is simulated using PFEM. The adopted approach builds on our previous PFEM developments [17], where the solid is modelled as a fluid constrained in motion, i.e. without displacement. This approach is widely used in simulations featuring phase change phenomena, e.g. in additive manufacturing [29]. For this reason, the PFEM submodel considers the aluminium as an incompressible Newtonian fluid in the liquid state, while the solid behaviour is approximated using the Carman–Kozeny equation, i.e. above the liquidus temperature (T_{liq}) the aluminium particles behave as a fluid, below the solidus temperature (T_{sol}) the particles' motion is blocked, and between T_{sol} and T_{liq} the flow is penalised to represent the mushy zone. This condition is governed by the following system of equations:

$$\rho \, \frac{d\mathbf{v}}{dt} - \mu \, \Delta\mathbf{v} + \nabla\text{p} = \rho \, \boldsymbol{b} + \boldsymbol{s} \qquad (5\text{a})$$

$$\nabla \cdot \mathbf{v} = 0 \qquad (5\text{b})$$

$$\rho \, c_{\text{p}} \, \frac{dT}{dt} + \nabla \cdot \boldsymbol{q} = L \qquad (5\text{c})$$

where $\mathbf{v}$ is the velocity vector, μ is the dynamic viscosity, Δ is the Laplacian operator, p is the pressure, and $\boldsymbol{b}$ is the gravitational acceleration vector. Natural convection is accounted for by the Boussinesq approximation, i.e. the density in the

body forces term is updated as a function of the temperature.

In Eq. (5), phase change is taken into account in the terms L and $\boldsymbol{s}$. The first one is the latent heat of fusion while the second one originates from the Carman-Kozeny equation and allows to shift the particle behaviour between the liquid and solid states. These terms are defined as:

$$L = -\rho \, \frac{\partial f_l}{\partial T} \, \frac{dT}{dt} \, L_{\text{m}} \qquad (6\text{a})$$

$$\boldsymbol{s} = c_{\text{ck}} \, \frac{(1 - f_l)^2}{\epsilon_{\text{ck}} + f_l^3} \mathbf{v} \qquad (6\text{b})$$

where L_{m} is the latent heat of fusion, f_l is the liquid fraction, and c_{ck} and ϵ_{ck} are user defined parameters, such that, c_{ck} must be large so that $\boldsymbol{s}$ results in a large number absorbing all the momentum when $f_l \to 0$, and ϵ_{ck} must be small to avoid afecting the momentum equation when $f_l \to 1$, but big enough to prevent numerical singularities when $f_l = 0$. The liquid fraction is defined as:

$$fl = \begin{cases} 1 & \text{, for } T \geq T_{\text{liq}} \\ \dfrac{T - T_{\text{liq}}}{T_{\text{liq}} - T_{\text{sol}}} & \text{, for } T_{\text{sol}} < T < T_{\text{liq}} \\ 0 & \text{, for } T \leq T_{\text{sol}} \end{cases} \qquad (7)$$

Thus, if the particle temperature is higher than T_{liq}, then $\boldsymbol{s}$ becomes zero and the flow is governed by the Navier-Stokes equation. If the temperature is lower than T_{liq}, the term becomes negative, penalising the flow by acting as a momentum sink to the point of consuming all the momentum when the temperature drops below T_{sol}. The reader is referred to [17] for further details on the descriptions of $\boldsymbol{s}$, L and f_l.

The aluminium plate is discretised in space using discrete particles, while the weak form of the governing equations are discretised with linear triangular finite elements generated from a Delaunay triangulation of the particles. The momentum (5a) and continuity (5b) equations are solved in a monolithic velocity-pressure formulation that uses implicit Backward Euler as time integration scheme. Given the LBB (Ladyzhenskaya-Babuška-Brezzi) condition to be satisfied and the use of linear elements with the same order of interpolation for velocity and pressure, PSPG stabilization (Pressure-Stabilizing Petrov-Galerkin) is adopted.
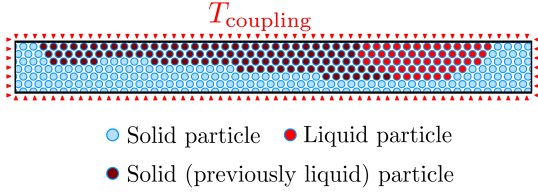
Fig. 5 Thermal boundary condition of the PFEM submodel and ilustration of the space discration using particles.

The discretised governing equations are omitted in this manuscript and the reader is referred to [30, 31] for further details.

Dirichlet boundary conditions are applied on the entire boundary of the aluminium plate. Specifically, particles located all along the boundary are fixed in all degrees of freedom, including particles that are in the liquid state, i.e. no-slip condition for the convective flow. In addition, a temperature T_{coupling} is also imposed on the boundaries, as shown in Fig. 5. This temperature depends on the solution obtained in the FEM model. Thus, the two models, FEM and PFEM, are coupled. The coupling scheme is explained in the following subsection.

It is worth noting that the Eqs. (5) are formulated in a Lagrangian framework, i.e. the finite element mesh is deformed according to the resulting velocity field. To avoid excessive element degradation, a new Delaunay triangulation is applied at each time step. In addition, particle arrangement is updated at each time step to guarantee a homogeneous distribution of particles in the domain. At the same time, a discretisation refinement is applied as a function of the melting temperature in order to better capture the melt pool boundary. For further details on the remeshing process of PFEM, the reader is referred to [30, 32].

2.3 FEM-PFEM coupling

The FEM and PFEM solvers are coupled by a Dirichlet-Neumann scheme, where the nodal temperature and displacement obtained from the FEM solver are imposed as a Dirichlet condition on the PFEM solver, while the heat flux and reaction forces obtained from the PFEM solver are imposed as a Neumann condition on the FEM solver. An illustration of this procedure is shown in Fig. 6.

Denoting as Γ the FEM/PFEM interface, as $\mathcal{F}$ the operator retrieving the FEM solution at Γ, as $\mathcal{P}$ the operator retrieving the PFEM solution at Γ, and taking the thermal coupling for the explanation, then:

$$T_{\text{FEM}}^{\Gamma} = \mathcal{F}(q_{\text{coupling}}) \tag{8a}$$

$$q_{\text{PFEM}}^{\Gamma} = \mathcal{P}(T_{\text{coupling}}) \tag{8b}$$

where T_{FEM}^{Γ} and q_{PFEM}^{Γ} are the solution of the FEM and PFEM solvers, respectively, while q_{coupling} and T_{coupling} are the coupling boundary conditions imposed on the FEM and PFEM solvers, respectively. In case the finite element meshes are coincident at the Γ interface, then $T_{\text{coupling}} = T_{\text{FEM}}^{\Gamma}$ and $q_{\text{coupling}} = q_{\text{PFEM}}^{\Gamma}$ (as typed in Fig. 6, Coupling box). However, this work includes an adaptive mesh refinement in the PFEM solver to capture the solid-liquid interface of the melt pool, which evolves and moves throughout the simulation. Therefore, having in general non-coincident meshes, solutions must be projected onto the Γ interface. Denoting as **P** the projection matrix, with subindices FP and PF to indicate projection from FEM-to-PFEM and from PFEM-to-FEM, respectively, then the coupling condition between solvers can be written as:

$$T_{\text{coupling}} = \mathbf{P}_{\text{FP}}\, T_{\text{FEM}}^{\Gamma} \tag{9a}$$

$$q_{\text{coupling}} = \mathbf{P}_{\text{PF}}\, q_{\text{PFEM}}^{\Gamma} \tag{9b}$$

Then, replacing the solution by the extractor operator:

$$T_{\text{coupling}} = \mathbf{P}_{\text{FP}}\, \mathcal{F}(q_{\text{coupling}}) \tag{10a}$$

$$q_{\text{coupling}} = \mathbf{P}_{\text{PF}}\, \mathcal{P}(T_{\text{coupling}}) \tag{10b}$$

a system of two unknowns (T_{coupling} and q_{coupling}) is obtained. The system can be treated as a fixed-point problem and be solved by many algorithms. Specifically, this work uses an Inverse Least Squares (ILS) algorithm, while the projection matrix **P** is built using radial basis functions. For details on the ILS-based solution scheme and for the construction of the projection matrix **P**, the reader is referred to [30, 33] and [20], respectively.

Note that the mechanical coupling between FEM and PFEM applies in a similar way as
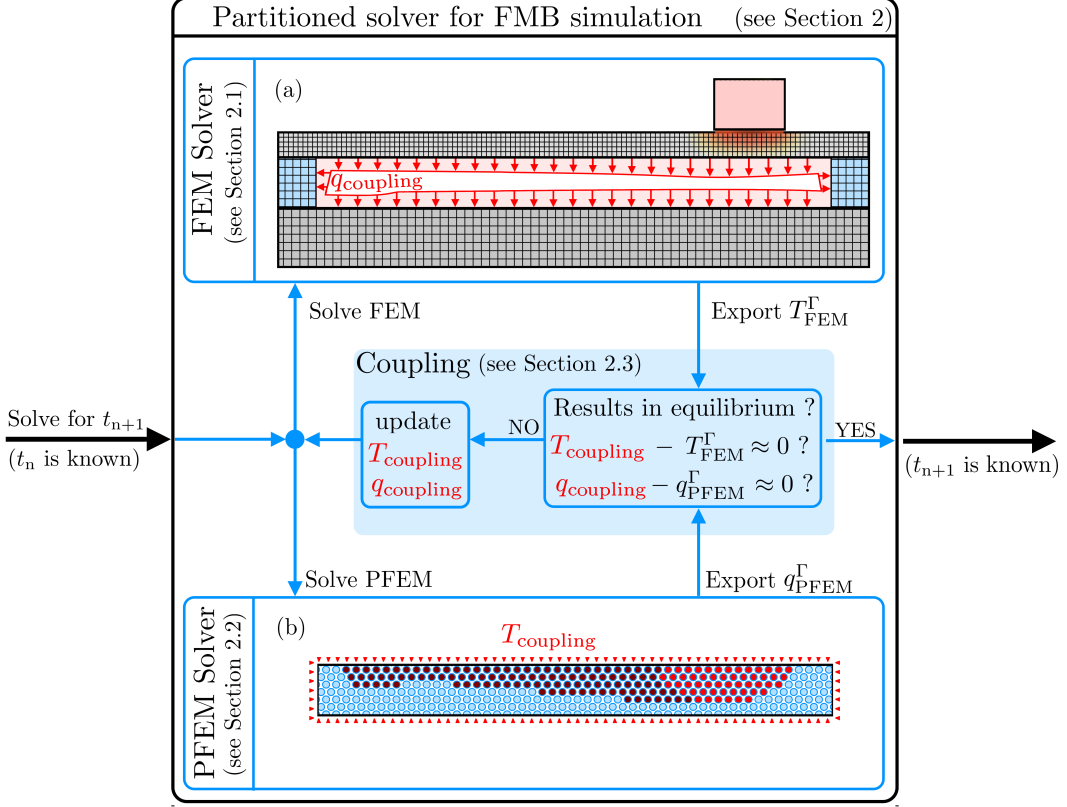
Fig. 6 Illustration of the proposed numerical approach to simulate the FMB process. (a) Domain solved by the Finite Element Method (FEM). (b) Domain solved by the Particle Finite Element Method (PFEM). The light blue box represents the coupling between the FEM and PFEM solvers in a Dirichlet-Neumann approach. Γ denotes the interface between the FEM and PFEM models (see Fig. 2). Only the thermal part of the coupling is illustrated here.

described above, but providing displacements to the PFEM submodel and returning forces to the FEM submodel. However, since the displacements of the aluminium plate are blocked in the PFEM submodel, the coupling between FEM and PFEM is equivalent to blocking the displacements of the FEM/PFEM interface in both submodels.

Having presented the submodels and the coupling strategy to simulate the FMB process, the following section explores different aspects of the FMB and compares results from FEM+PFEM simulations against experimental data.

3 Simulation results of the FMB process

This section gathers the results of several simulations of the FMB that aim to reveal the scope and limitations of the proposed methodology. The section first presents the chosen experimental

setup of the FMB process and the set of physical parameters involved in the FEM and PFEM submodels. Then, it discusses the simplification in dimension (2D), analyses the influence of different model variables and finally it comments on the effect of considering the convective flow in the melt pool.

3.1 Experimental and numerical FMB setup

The FMB process is carried out to weld a structural steel plate (S235) and an aluminium plate (AA1050) of 1.5 mm and 3.0 mm thickness, respectively, while the backing plate is 10.0 mm thick. The plates are 200 mm long and 80 mm wide. The tool is 16 mm in diameter and its axis of rotation is placed 25 mm from the left edge of the aluminium plate. All experimental tests account for 150 mm of horizontal displacement for the tool (d_{travel} in Fig. 1).
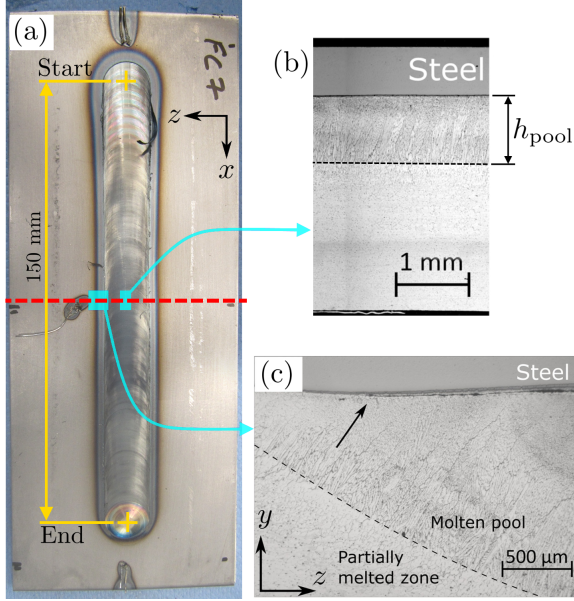
Fig. 7 FMB experimental sample. (a) The steel plate is observed from the top. The heat affected zone and the damage caused by friction are visible on the steel plate. (b) Typical views by light microscopy. Subfigures (b) and (c) are retrieved from [4].

From the experimental tests, the geometry of the melt pool is measured at the middle of the weld bead, as illustrated in Fig. 7a. The thickness and width of the weld bead is measured under a microscope, after cutting, polishing and etching the cross-section. Typical images are shown in Figs. 7b and 7c.

Regarding the physical parameters of the FEM model, the thermal conductance (see Eq. 1) is defined by $H_v = 500$, $w = 1.25$ and $h_{c0} = 250 \text{ kW}/(^\circ\text{K}m^2)$, whose orders of magnitude were gathered from [34, 35]. The tool is controlled in position as indicated in the previous section, with a penetration distance $d_{tool} = 37\mu m$ (see Fig. 4).

In the thermal model, coefficients defining boundary conditions in the top surface of the steel plate are defined as $\epsilon_{rad} = 0.5$ and $h_{conv} = 50$ $\text{W}/(^\circ\text{K}m^2)$, while the side surfaces of all plates as $\epsilon_{rad} = 0.3$ and $h_{conv} = 25 \text{ W}/(^\circ\text{K}m^2)$. Orders of magnitude for these values have been gathered from [36, 37]. The thermal conductivity and the specific heat capacity are considered temperature-dependent and are given in Appendix A. On the other hand, the Young's modulus of the steel,
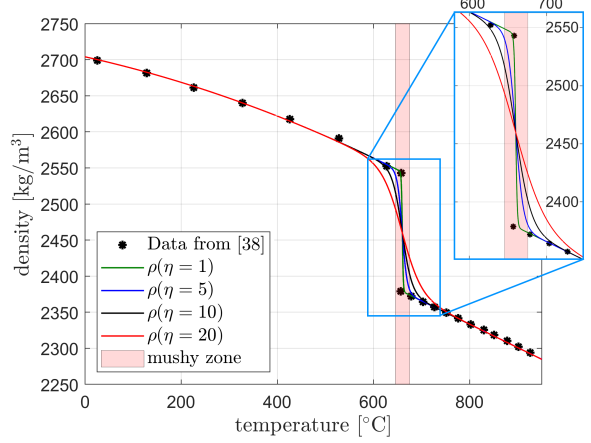
Fig. 8 Temperature-dependent density curves. η represents a parameter defining the smoothness of a Heaviside function defined in Appendix A.

aluminium and backing plates are considered constant with respect to temperature and equal to 210 GPa, 70 GPa and 190 GPa, respectively. Densities are likewise assumed constant throughout the simulation and defined as 7850, 2700 and 8000 kg/m^3, for the steel, aluminium and backing plates, respectively.

Given that phase change takes place in the aluminium plate, an abrupt transition of physical parameters is present in the PFEM model. This transition has been relaxed using smoothed Heaviside functions. The smoothing procedure is described in Appendix A and it is illustrated below for density only.

Following the Boussinesq approximation, densities in the body force term of the momentum equation and in the heat equation are temperature dependent. The temperature dependency is obtained by fitting the experimental points given in [38], which are illustrated as black dots in Fig. 8. Taking the solid and liquid regions separately, the curves that fit the experimental points are:

$$\rho = \begin{cases} -1.418 \cdot 10^{-4}\, T^2 \ldots \\ \quad \ldots - 0.1487T + 2704 & \text{, if } T < 660^\circ\text{C} \\[2mm] 2378.7 - 0.324\,(T - 660) & \text{, if } T \geq 660^\circ\text{C} \end{cases}$$

(11)

where T is given in $^\circ$C and 660 $^\circ$C corresponds to the melting temperature [39]. The density jump in the phase-change zone (≈ 660 $^\circ$C) is smoothed following the procedure described in Appendix A.

9
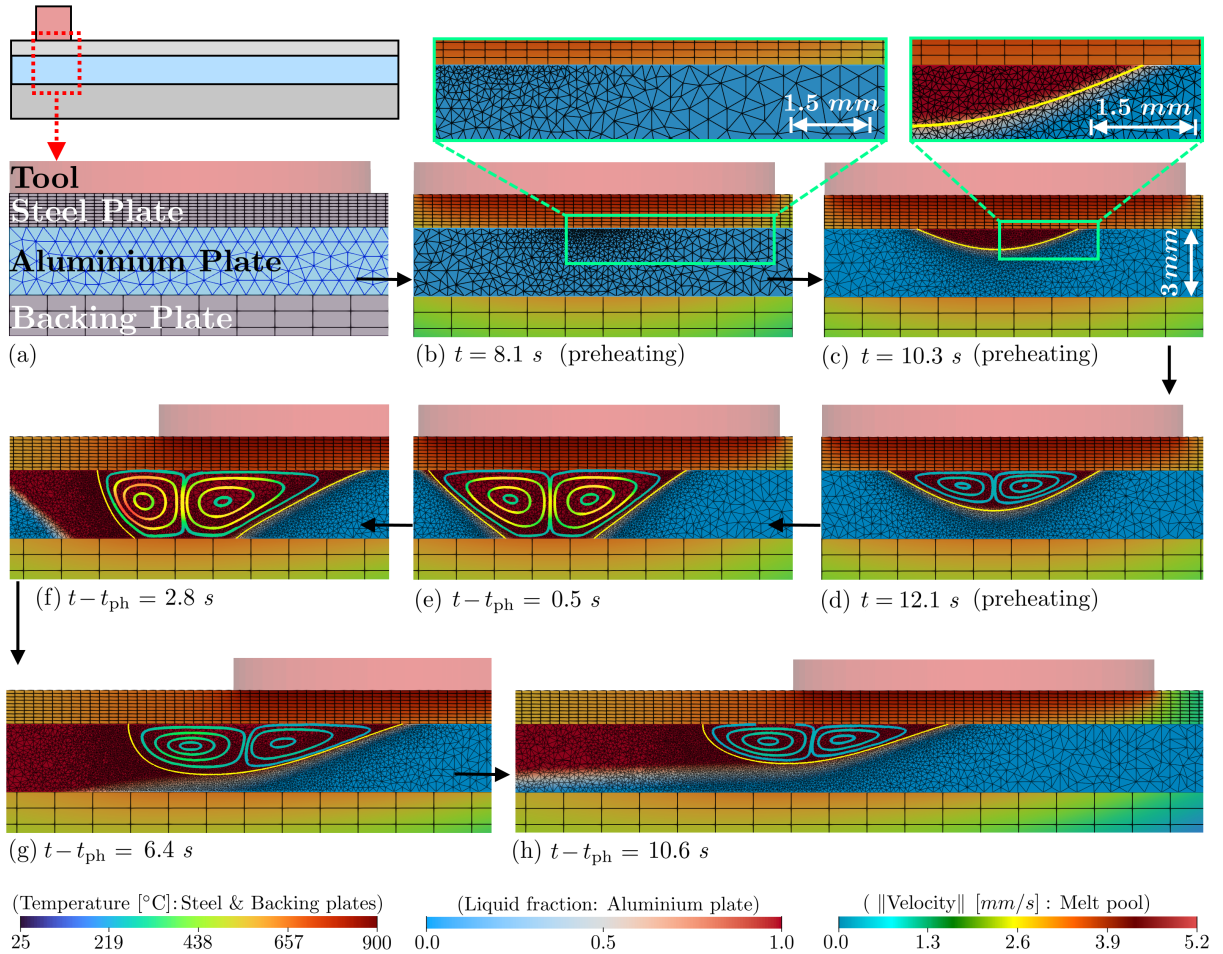
Fig. 9 Simulation of the FMB process using a partitioned FEM + PFEM approach. (a) The initial discretisation. (b) Temperature in the aluminium plate approaches the melting point and element size is adapted in the PFEM zone. (c) Melt pool appears. (d) Melt pool starts flowing due to natural convection. (e) The preheating phase is completed and the tool begins to move horizontally while the melt pool reaches the full thickness of the aluminium plate (3 mm). (f) The melt pool loses its symmetry and begins to follow the tool. (g) The melt pool reduces its size due to the fast displacement of the tool movement. (h) The geometry of the melt pool begins to stabilize marking a stationary regime of the FMB process. Above the color bars are indicated which plates they correspond to.

That is, the polynomial equations that fit the experimental points in the solid and liquid range are multiplied by a smoothed Heaviside function that depends on a parameter η, obtaining the curves shown in Fig. 8. In this work, $\eta = 5$ is used. Similarly, the dynamic viscosity μ, the specific heat capacity c_p and the thermal conductivity governing the heat flux ($\boldsymbol{q}$) are also temperature-dependent and smoothed in the phase-change zone. The fitting curves for these parameters are given in Appendix A.

According to the relaxation scheme, the chosen solidus and liquidus temperatures are $T_\mathrm{sol} = 645°$C and $T_\mathrm{liq} = 675°$C, respectively. This results in the mushy zone shaded in pink in Fig. 8, which extends over 30 °C, similar to the temperature range reported in [40]. In this transition zone, the heat absorbed/released is defined by a latent heat of fusion of $L_m = 400$ kJ/kg (obtained by rounding the value reported in [38]). On the other hand, the momentum sink that models phase change in the Navier-Stokes equation is defined by $c_\mathrm{ck} = 10^9$ kg/($m^3\ s$) and $\epsilon_\mathrm{ck} = 10^{-3}$ (obtained from numerical experiments).

The final outcome of this partitioned FEM + PFEM approach is illustrated in Fig. 9. There, a typical 2D simulation of the FMB process is

shown. This one is obtained with a preheating time t_{ph} of 15 s, a tool temperature $T_{tool} = 867$ °C, and $v_{tool} = 200$ mm/min. In this example, and in all examples reported in this work, space discretisation is kept fixed in the FEM submodel throughout the simulation, while it is modified in the PFEM submodel according to the melting temperature to better capture the fluid-solid interface. In the PFEM sub-model, specifically, the element size is interpolated with respect to temperature, between room and melting temperature. Thus, the initial element size is 0.75 mm (at room temperature) and 0.1 mm in the mushy zone (around melting temperature). Fig. 9a displays the initial discretisation of the FEM and PFEM sub-models, and Fig. 9b shows a mesh refinement before the appearance of the melt pool (Fig. 9c).

In the preheating phase, the tool remains stationary and the aluminium plate is heated to the point of generating a melt pool (Figs. 9b-9d). After some time and once the melt pool reaches a significant size, flow by natural convection becomes visible (Fig. 9d). If the supplied heat is excessive, the full thickness of the plate will be melted (Fig. 9e). However, moving the tool horizontally also drives the movement of the melt pool, changing its geometry with respect to the preheating phase (Figs. 9f-9h). It is important to note that figures in this work show different colour scales in the same snapshot. In particular, the aluminium plate shows the maximum value of the liquid fraction that the particles have reached during the simulation. This helps to visualise the depth of the melt pool reached before the snapshot time. Additionally, the melt pool contour is drawn with a yellow line (and white in the some other figures) to illustrate the melt pool geometry at the snapshot time.

3.2 Choice of 2D methodology

As mentioned in section 2, this work is constrained to 2D for computing time considerations. To justify this simplification and to illustrate the representativeness of the 2D model, a comparison of 2D and 3D solutions is given below.

As stated previously, we set an element size of 0.1 mm around the melting temperature in order to capture the mushy zone. However, this element size is not suitable for our 3D computational environment due to prohibitive computational time.

(a)

(b) Top view 3D PFEM model

(c) Side view 3D model
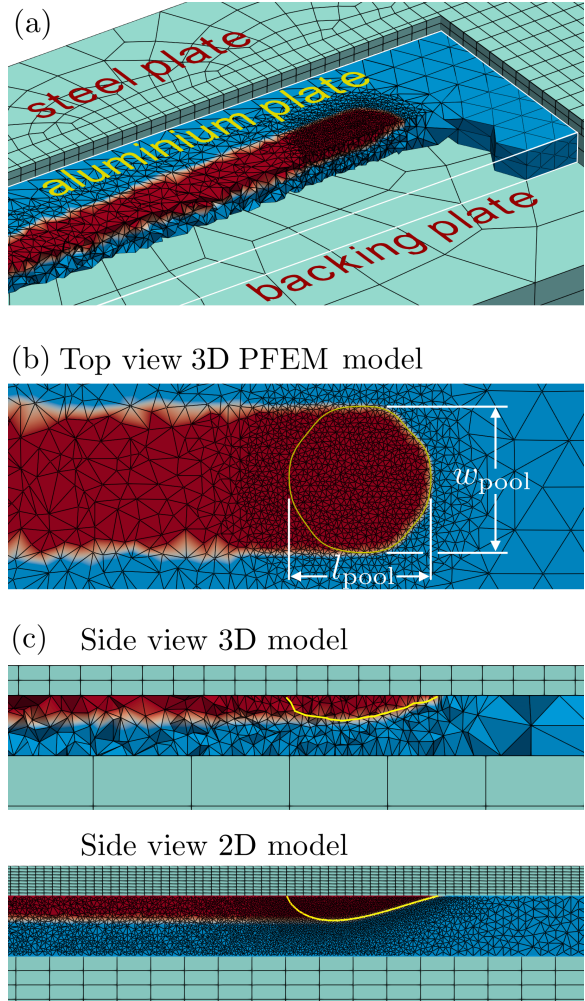
Side view 2D model

Fig. 10 (a) Perspective view of the 3D model, with sectioning of the steel and aluminium plates to illustrate the spatial discretisation. (b) Top view denoting the width and length of the melt pool. (c) Side view of the symmetry plane of the 3D model, placed above the 2D model for comparison. The aluminium plate shows the liquid fraction history.

Instead, the 3D PFEM model used in the comparison is discretised with tetrahedral elements ranging from 3.0 mm at room temperature to 0.25 mm in the mushy zone. Similarly, element size in the 3D FEM model is 3 times larger than in the 2D model. Fig. 10c allows a comparison between 2D and 3D spatial discretisations.

As in the 2D model, heat is transferred to the steel plate by contact and by imposing the tool temperature T_{tool}. However, the tool is cylindrical in the 3D case (diameter 16 mm) and much smaller than the width of the plates (80 mm), so

11

the heat provided to the steel plate is reduced compared to the 2D case. As a result, to obtain the same depth of molten aluminium, the tool temperature in the 3D model must be higher than in the 2D case. For instance, numerical experiments showed us that a $T_{\text{tool}} = 1627\ ^\circ C$ in 3D leads to a melt pool depth similar to that obtained with $T_{\text{tool}} = 857\ ^\circ C$ in 2D, when $v_{\text{tool}} = 200\ mm/min$ and $t_{\text{ph}} = 5\ s$. Fig. 10c shows a comparison of melt pools obtained with the 2D and 3D models using the mentioned parameters. Snapshots corresponds to 55 mm of tool displacement.

As described in the previous example, when the tool starts its horizontal displacement, the melt pool loses the symmetry evidenced in the preheating phase. Specifically, the molten material accumulates at the rear zone relative to the moving direction, resulting in a belly-like shaped melt pool. Interestingly, this observation also applies to the 3D model when considering the side view of the plane of symmetry, as shown in Fig. 10c.

It can be noticed in Fig. 10c that the coarse discretisation in the 3D model is not able to accurately capture phase changes in the mushy zone, and yet the model is computationally demanding. Specifically, on a computer with 10 cores (20 threads) and an *Intel(R) Core(TM) i9-10900X CPU @ 3.70GHz* processor, the computation time of the 3D model is 126 hours, while the 2D model takes about 8 hours. In other words, the 3D model takes about 15 times longer than the 2D model, which makes it impractical to perform a parametric study on the thermal boundary conditions or the parameters involved in the FMB process. The prohibitive computation time, even for a coarse mesh, is largely attributable to the fact that the Navier-Stokes equations are formulated in a monolithic system and solved with a direct solver.

It was mentioned in the previous subsection that the melt pool width is measured experimentally, which will be denoted as w_{pool}. However, given the geometrical limitation of the 2D model, it is not possible to obtain the melt pool width but its length, which will be denoted as l_{pool}, as shown in Fig. 10b. On the other hand, as the physical properties of steel and aluminium are isotropic, that the tool is circular, and that the steel plate is rather thin, it is reasonable to think that $w_{\text{pool}} \approx l_{\text{pool}}$. This can be verified in the 3D result illustrated in Fig. 10b. This shows that

the melt pool is quite circular when viewed from the top, and although we have reported only one 3D example here, we can indicate that this 3D model was verified for different thermal boundary conditions and it was consistently observed that $w_{\text{pool}} \approx l_{\text{pool}}$. Thus, given the computing time issue of the 3D model and that the 2D model is topologically representative of the symmetry plane of the 3D model, a 2D study seems the best option.

In the following, the same experimental and numerical setup is used in all the examples of this work, but with variations in the tool conditions, such as travel speed (v_{tool}), rotating speed (ω_{tool}) and applied force (f_{tool}). Specifically, four aspects are examined hereafter. First, the relationship between the operating conditions and the tool temperature imposed on the model. Second, the influence of the preheating time, third, the effect of the travel speed, and finally, the effect of accounting for the convective flow in the melt pool.

3.3 Tool temperature

As mentioned in Section 2.1, the heat source in the FEM model is a rigid tool at elevated and constant temperature. To correlate the numerical temperature and the real tool conditions, we proceed to find the numerical set that leads to the experimental melt pool depth. Specifically, three operation conditions are compared in this study. All three use the same travel speed, $v_{\text{tool}} = 200$ mm/min, but differ in the rotational speed ω_{tool} and the applied force f_{tool}. The three conditions are summarised in Table 1, with labels T1, T2 and T3.

Several simulations are carried out with a constant displacement of 200 mm/min and temperatures T_{tool} between 800 and 1000 $^\circ C$. Clearly, the higher the T_{tool} temperature, the deeper the resulting melt pool. Fig. 11 illustrates this effect, while Fig. 12 relates the melt pool depth to the tool temperature. Below 805 $^\circ C$, no melt pool is generated, while above 925 $^\circ C$, the aluminium plate is melted through all its thickness. This leaves an operating range of approximately 110 $^\circ C$ for an efficient process.

The numerical tool temperature can be established by matching the melt pool depth with the

12

Table 1 Summary of the four experimental tests that are compared with the numerical results. T1 to T3 are covered in section 3.3, while T4 in section 3.5.
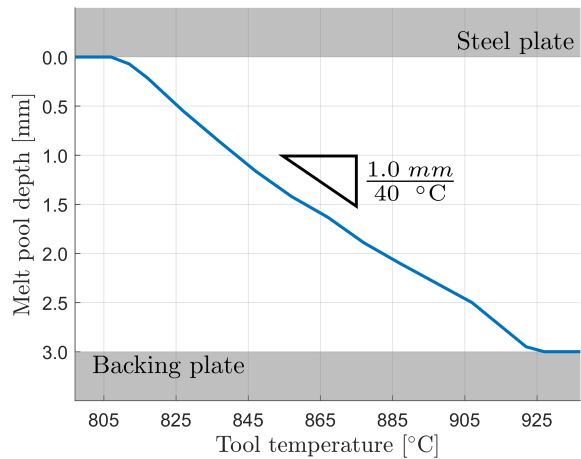
| Test	Experiment					Simulation		
	v_{tool} (mm/min)	ω (RPM)	f_{tool} (kN)	h_{pool} (mm)	w_{pool} (mm)	T_{tool} (°C)	h_{pool} (mm)	l_{pool} $(mm, \%w_{pool})$
T1	200	1800	6	1.3	8.5	852	1.3	8.6 , +1%
T2	200	2000	6	2.2	10.7	892	2.2	12.7 , +18%
T3	200	2000	7	3.0	10.9	926	3.0	15.0 , +37%
T4	250	1800	6	0.7*	5.8*	852	0.7	6.4 , +10%

∗ Average of two experimental tests.
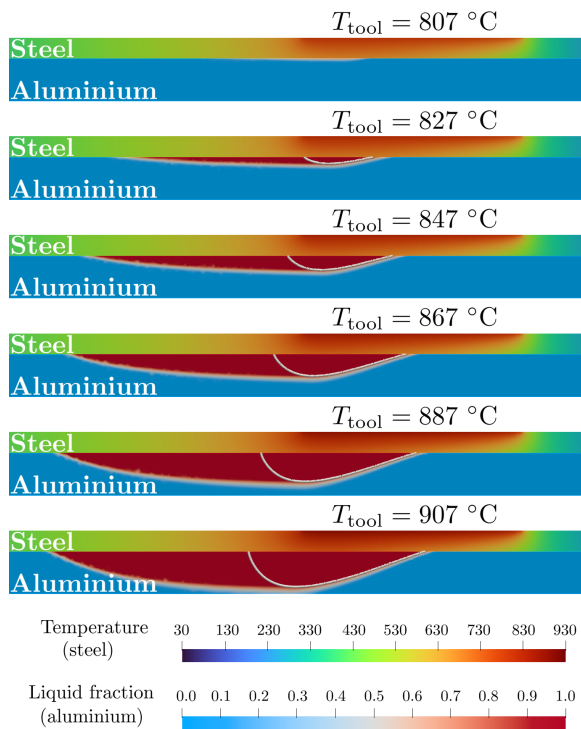
Fig. 11 Simulations for different tool temperatures but same travel speed of 200 mm/min. From each simulation, the melt pool geometry is measured to create the graph in Fig. 12.

Fig. 12 Melt pool depth for different tool temperatures (T_{tool}). Note that the ordinate axis is reversed for illustrative purposes. The grey zones represent the steel and backing plates. The graph is built for $v_{tool} = 200\ mm/min$.

experimental tests. Thus, the obtained tool temperature (T_{tool}) and melt pool length (l_{pool}) are reported in Table 1 (rows T1, T2 and T3, column "Simulation"). Next to the melt pool length (l_{pool}) in Table 1, it is shown the percentage variation with respect to the melt pool width measured experimentally. In the T1 test, which supplies the least energy to the steel plate, a melt pool of about one third the thickness of the aluminium plate is obtained, and a length that is very similar to the width (1% difference). As more energy is put into the system, a greater difference between the melt pool width and length becomes apparent. This can be due to a number of factors. For example, inaccurate thermal boundary conditions due to the effect of reducing the problem dimension to 2D, to ignoring the thermal contact resistance, or effects introduced by tool damage. In fact, the high local pressures generated by the tool deform the steel plate in the thickness, and could even deflect the plate away from the aluminium plate, as illustrated in Fig. 13 (which represents a pure-FEM model). This would reduce the thermal contact conductance outside the pressure cone and thus narrow the melt pool. However, since this work does not consider a constitutive law for the solid
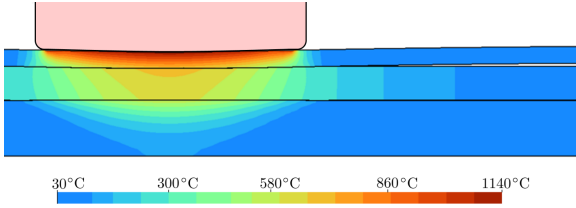
Fig. 13 Illustrative solution from a pure FEM model of the FMB process. The three plates are modelled as deformable solids that can interact through a contact algorithm. Deformation through plate thickness and bending of the steel plate are observed. The displacements are magnified by a factor 10 for visualisation purposes.

phase of PFEM, it is not possible to consider deformations in the aluminium plate. Regarding the tool, it is progressively damaged and deformed during FMB. The base of the tool loses its flatness and takes a conical shape, while the rim of the base develops a flash collar, similarly to the flash collar developed in RFW (Rotary Friction Welding). This progressive geometrical transformation of the tool was not considered in this work to avoid including additional free-parameters that would have had to be fine-tuned on the model.

As the numerical model is more reliable for low loading conditions on the tool, the following sections only consider the operating condition T1 given in Table 1.

3.4 Preheating time identification

As explained in Section 2.1, the preheating process starts when the tool comes into contact with the steel plate and ends when the tool starts its horizontal displacement. During this first period, the tool penetrates linearly in the plate for an imposed distance (37 μm). The longer the preheating time, the more energy is delivered to the system before the tool starts to move horizontally. To evaluate this effect, several simulations are run using the same tool temperature ($T_{tool} = 852$ °C), the same travel speed ($v_{tool} = 200$ mm/min), same penetration distance, but different preheating times. Fig. 14 shows the melt pool trace on the aluminium plate of some simulations. Clearly, the longer the preheating time, the larger the melt pool at the beginning of the FMB process. However, the melt pool geometry stabilises 22 seconds after displacing the tool. Undoubtedly, the stability of the melt pool comes from the assumption of a constant temperature under the backing

plate and a tool at a constant temperature. These assumptions are unlikely representative of real FMB conditions, but permit to conclude that it is possible to achieve a stationary regime in the FMB process under optimal conditions.

The preheating stage in the experimental test reaches the penetration distance in several seconds in order to raise the temperature gradually and prevent damage to the plate or tool. The duration of this process depends on the time required to reach some incandescent colour and, among other factors, on the condition of the tool and the thermal boundary conditions (T_{tool}, T_{room}, initial plate temperature, etc). As these aspects may vary from one test to another, replicating the preheating process in the simulation is challenging and thus, it is also difficult to compare temperature with the experiments. Therefore, in order to compare temperatures against experimental measurements, temperature from simulations with different preheating times are recorded at 8 mm from the left edge to match the position of an experimental thermocouple that is placed at the symmetry line. The aim is to obtain the preheating time that leads to a maximum temperature equal to that of the experimental record. As shown in Fig. 15, the resulting preheating time in the simulation is 4 seconds (blue curve). From the figure it is observed that although temperatures from the experiment and simulation ($t_{ph} = 4$ s) are completely different in the preheating phase, they are very similar during the horizontal displacement phase, which validates the representativeness of the boundary conditions in the 2D model.

3.5 Effect of the travel speed

Having identified the tool temperature and preheating time that approaches the real operation conditions of the FMB process, we now proceed to verify their accuracy using a different travel speed. For this purpose, the operating conditions of test T1 (Table 1) are used, but with a travel speed of 250 mm/min. The experimental test is carried out in duplicate with tools in different states, one new and the other one already used in some tests.

The experimental and simulation temperatures are shown in Fig. 16, while the melt pool geometry is reported in the fourth row of Table 1
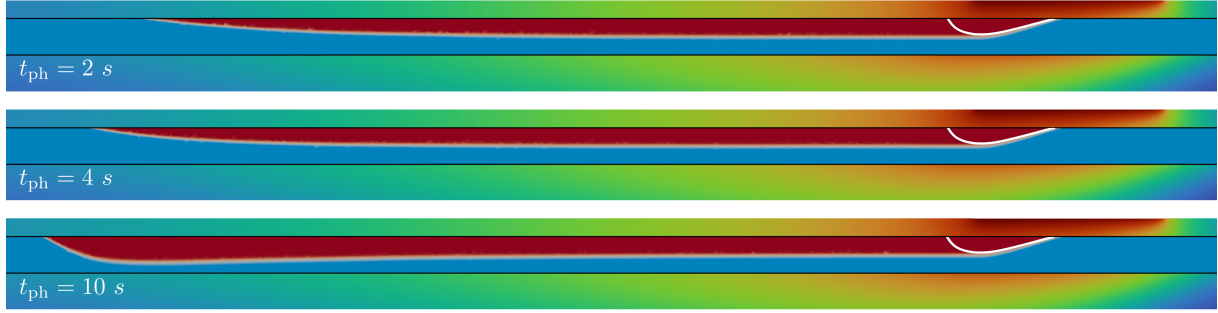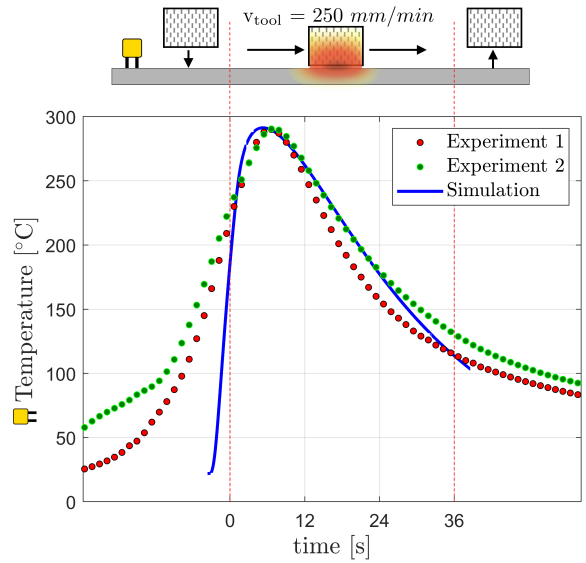
Fig. 14 Simulations for different preheating times (t_{ph}) but same tool temperature ($T_{\text{tool}} = 852\ °$C) and travel speed ($T_{\text{tool}} = 200\ mm/min$). All the snapshots are taken at $24\ s$ after starting the tool displacement.
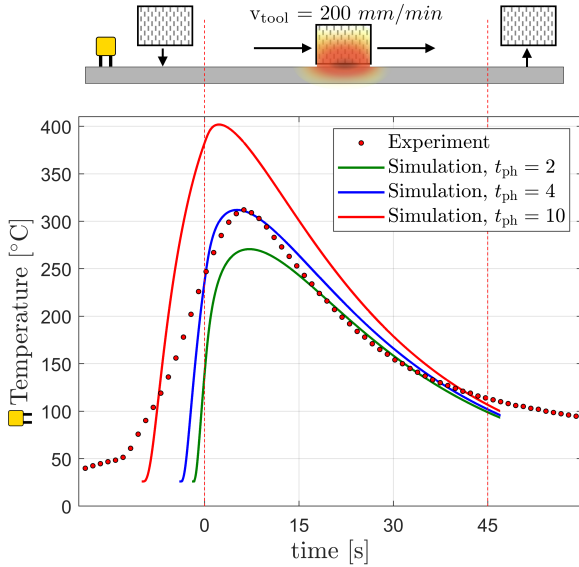
Fig. 15 Temperature of a thermocouple placed between the left edge of the plate and the initial position of the tool, as shown in the sketch over the graph. Three simulations are plotted with different preheating times t_{ph} (given in seconds). $t_{\text{ph}} = 4\ s$ leads to the same maximum temperature recorded experimentally.

Fig. 16 Temperature of a thermocouple placed between the left edge of the plate and the initial position of the tool, as shown in the sketch over the graph. The simulation uses a preheating time of $4.0\ s$.

(test T4). It is clear that both, the melt pool geometry and the temperature of the thermocouple during tool displacement, are well approximated by the FEM+PFEM model. Also, recorded temperatures show that tool condition influences the preheating cycle. Approximately the same maximum temperature is obtained in both experiments, but experiment 1, which employs a new tool, records a lower temperature at the thermocouple during most of the FMB process.

Despite the numerous complex phenomena involved in the FMB process, it can be noted that

the temperature field at the thermocouple location and the geometry of the melt pool are well approximated by the model in the chosen operating range. The advantage of having a reliable model is the possibility to predict the behaviour of the FMB process under different operating conditions at a much lower cost than doing it experimentally. For example, it is possible to run several simulations with variations in the travel speed and to obtain the melt pool depth for each case. This results in the graph in Fig. 17. As expected, the slower the travel speed, the higher the energy delivered to the system, and hence the larger the melt pool. On the other hand, a
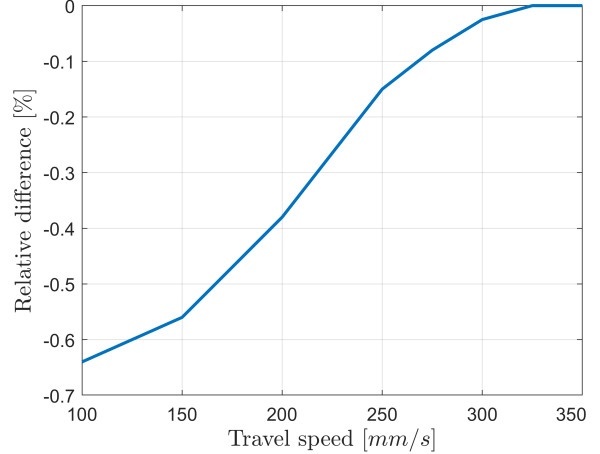
15
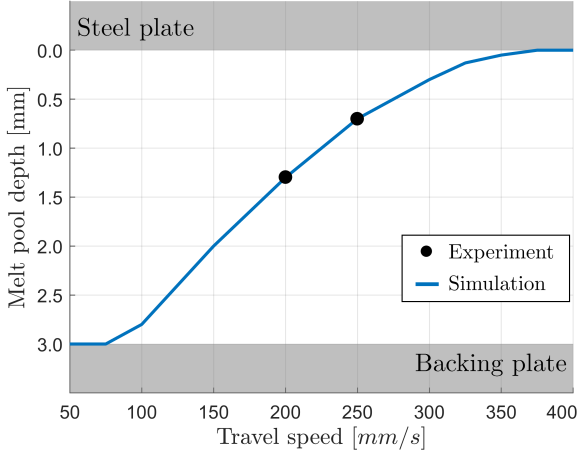
Fig. 17 Melt pool depth for different tool travel speeds (v_{tool}). Note that the ordinate axis is reversed for illustrative purposes. The grey zones represent the steel and backing plates. The graph is built for $T_{tool} = 852$ °C.

Fig. 18 Relative difference in melt pool depth between flowing and non-flowing melt pool models.

very high travel speed does not provide enough energy to melt the aluminium plate. According to the model, the operating range would be $75 \leq v_{tool} \leq 350$ mm/min, for $\omega_{tool} = 1800$ RPM and $f_{tool} = 6$ kN. Although this work does not include an experimental study on the travel speed over a wide range, it can be seen that the operating range obtained by FEM+PFEM is very close to that reported by other studies [41].

3.6 Flowing versus non-flowing melt pool

The purpose of making use of PFEM in this work is to take into account phase change and convective flow in the aluminium plate. Yet, it is possible to find in the literature works based on FEM that do not simulate the convective flow and simply modify the thermo-physical properties of the material to account for phase changes [4–6]. Given that there are no comparative works between models with flowing and non-flowing melt pools in the context of FMB, to the best of the authors' knowledge, it becomes worthwhile to provide this information.

To quantify the effect of convective flow, melt pool geometries without flow consideration are obtained for a tool temperature of 852 °C and different tool travel speeds. Thus, results can be compared with those obtained in the previous section. Fig. 18 shows the relative difference in melt pool depths between flowing and non-flowing

models. The same was done for the melt pool length, although it is omitted as the graph is very similar to that of the depth.

The negative values in Fig. 18 indicate that the melt pool size is smaller in the model that does not account for the convective flow. However, the percentage difference in depth is very small and arguably negligible, being less than 1% in absolute value. According to our examination, there are two reasons for this.

On the one hand, the horizontal displacement of the melt pool (or tool) is fast enough to avoid significant convective displacements. In fact, molten aluminium requires some seconds to gain momentum, which is hindered if the solidification-melting-solidification process takes place in a short time span. This can be seen in Fig. 19a, where melt pools of both models are compared for $v_{tool} = 100$ mm/min, which is a speed close to the lower bound limit due to the large melt pool size that is obtained. The figure shows the melt pool profile (yellow line), the velocity field inside the melt pool and the stream lines. In this condition, the tool and melt pool travel horizontally at 1.67 mm/s, while the molten aluminium has a maximum velocity of 2.8 mm/s according to our model, and a maximum travel distance of the order of 3 mm for the trajectory presented in Fig. 19a (red dashed line). For faster travel speeds v_{tool}, the melt pool size and molten aluminium displacements are smaller, and hence the difference between flowing and non-flowing melt pool models is smaller, as shown in Fig. 18.

16

On the other hand, temperature gradients in the melt pool are about 40 °C/1.5 mm, as shown in Fig. 19b. This is evidently small compared to, e.g. additive manufacturing, where huge temperature gradients are present, ranging from the melting point to the evaporation point over a fraction of a millimetre. An estimate of the Rayleigh (Ra) number can help quantify the relevance of natural convection in the FMB process. Ra can be written as the product of the Grashof number (Gr) and the Prandtl number (Pr), which are defined as:

$$Gr = \frac{g \, \beta \, \Delta T \, L_c^3 \, \rho^2}{\mu^2} \quad (12a)$$

$$Pr = \frac{\mu \, c_p}{\kappa} \quad (12b)$$

where β is the thermal expansion, L_c a characteristic length (e.g. the melt pool depth), and ΔT the temperature difference across the melt pool. Prandtl number depends only on the fluid properties, being $Pr \ll 1$ in liquid metals, meaning that the heat diffuses quickly. On the other hand, the Grashof number gives the relevance of buoyancy to viscous forces acting on the fluid, and depends on both physical and spatial variables.

The bigger Gr or Pr, the higher the Rayleigh number and the more relevant the heat transfer by convection. However, the Grashof number is restricted in the FMB process for operational reasons. The maximum depth for the melt pool is 3 mm (L_c), and the temperature difference in the melt pool is of the order of 60 °C (Fig. 19b). This indicates that $Ra \approx 200$ in FMB, which is relatively small compared to, e.g. $Ra = 1000$, which is commonly reported as relevant for natural convection. A study on the critical value of Ra in FMB is beyond the scope of this work, but at least it can be concluded that for the operating conditions considered in this work, the influence of natural convection is moderate on the melt pool geometry.

However, the weld quality is also determined, among other aspects, by the presence of brittle intermetallic compounds and residual stresses, which depend on the pressure field of the melt pool. This variable does not form part of this study because the fluid is incompressible in our model, resulting in unrealistic pressures as they only capture the height of the fluid column. Therefore, our
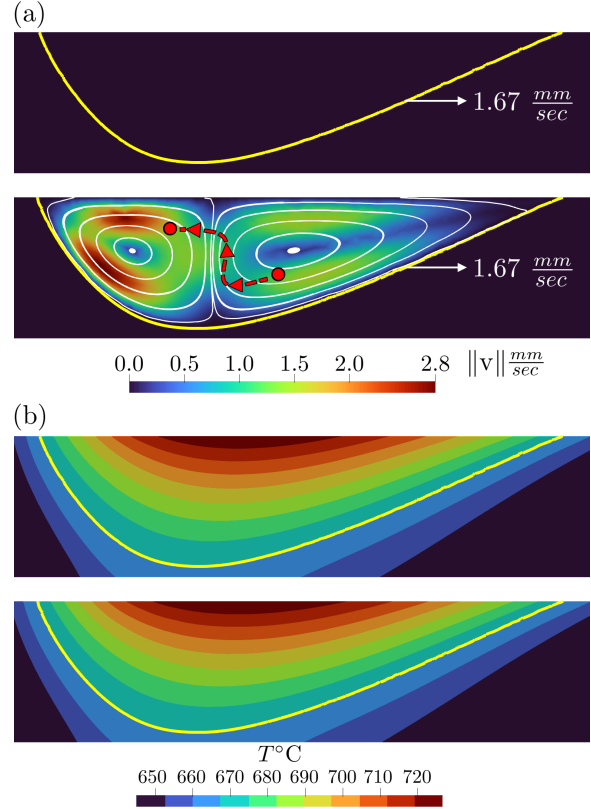
Fig. 19 Portion of the aluminium plate showing the stationary melt pool for $v_{\text{tool}} = 100$ mm/s and $T_{\text{tool}} = 852$ °C. Models without and with flow of molten aluminium are compared. (a) Velocity field and (b) Temperature field. The red dashed line in (a) illustrates one of the longest paths of particles present in the melt pool that move between the upper part (hot) and lower part (cold) of the melt pool. This path is obtained by placing 20 control particles across the plate thickness, which "float" on top of the mesh and whose displacements are driven by the velocity field of the mesh. The trajectory is traced using post-processing filters in Paraview.

future work on the simulation of weld joint quality will comprise a compressible fluid flow model for the melt pool as well as a constitutive law for the solid phase of PFEM.

4 Conclusions and perspectives

This work presents a new numerical methodology to simulate the FMB process. The strategy partitions the FMB process into two submodels, one solved by the Finite Element Method (FEM) and the other by the Particle Finite Element Method (PFEM). PFEM is used to simulate the phase

change in the aluminium plate and the convective flow within the melt pool. On the other hand, FEM is used to simulate the steel plate and the accompanying elements (tool and backing plate) that do not undergo phase change. The models are solved using two specialised in-house pieces of software, which are coupled by a third code. The adopted methodology along with numerical and experimental tests allow us to conclude the following:

- Although not representative of the geometry of the FMB process, a 2D model is able to provide accurate results of the melt pool geometry and surface temperature. This was verified by comparing experimental and numerical results.

- The preheating time (before the tool starts to move horizontally) has a local effect on the melt pool. In the numerical tests, i.e. under ideal thermal boundary conditions, a stationarity in the melt pool size is observed 20 s after the initiation of the horizontal tool displacement.

- The convective flow within the melt pool has a small influence on the heat distribution within the melt pool in the FMB process. This is due to the fact that the displacement of liquid metal is small in relation to the size of the melt pool, and that the temperature difference within the aluminium melt pool is not significant.

The present work was restricted to the geometry of the melt pool. However, to predict the weld quality, criteria for hot tearing and presence of brittle intermetallic compounds must be adopted. This will require a more realistic constitutive model of the solid phase in the PFEM model, in order to compute deformations and stresses. At the same time, the accuracy of the thermal model should be improved by feedback of more experimental data. This will demand an efficient and fast implementation of the 3D FEM+PFEM approach in order to perform the fitting of model parameters in a reasonable amount of time. Finally, it should be noted that the proposed methodology was assessed for the FMB process in the joining of aluminium and steel, however, it can be extended to other joining methods involving phase changes. These topics will be the subject of future research.

Conflict of interest. All authors declare that they have no conflicts of interest.

Appendix A Material properties

The thermo-physical properties of the three plates are temperature dependent. Experimental measurements of the material properties are gathered from the literature and fitted with polynomial functions denoted as þ. These functions are listed in Table A1.

To smooth the sharp transition of aluminium properties at the phase change, smoothed Heaviside functions are used. In a general way, the smoothed function defining a physical parameter with respect to temperature is denoted by $\bar{\text{þ}}$ and is defined as:

$$\bar{\text{þ}}(T) = \text{þ}_\text{s}\, \text{h}_\text{s} + \text{þ}_\text{l}\, \text{h}_\text{l} \, , \tag{A1}$$

where þ_s and þ_l are the fitted polynomial functions defining physical properties in the solid and the liquid phase, respectively. The functions smoothing the transition between þ_s and þ_l are defined as:

$$\text{h}_\text{s} = \bar{\text{h}}\,(\bar{a} + \bar{\text{h}}\,(1 - \bar{a})) \tag{A2a}$$

$$\text{h}_\text{l} = (1 - \bar{\text{h}})(1 + \bar{\text{h}}\,(1 + \bar{a})) \tag{A2b}$$

where $\bar{\text{h}}$ is the smoothed Heaviside function and $\bar{a}$ is the normalized property jump at the melting temperature (T_m), equal to 660 °C in this work. These are defined as:

$$\bar{\text{h}}(T) = \frac{1}{1 + \text{e}^{1/\eta\,(T - T_\text{m})}} \tag{A3a}$$

$$\bar{a} = \frac{\text{þ}_\text{s}(T_m) - \text{þ}_\text{l}(T_m)}{\text{þ}_\text{s}(Tm)} \tag{A3b}$$

The steepness of the smoothed Heaviside function is controlled by the parameter η. Fig. A1 illustrates its effect. The graph shows two polynomial functions that separately define an arbitrary

Table A1 Temperature-dependent thermal properties of steel, aluminium and backing plates. Units of κ, c_{v}, c_p and μ are, respectively, W/(m °C), J/(g °C) and mPa·s. Functions use temperature in °C. Experimental data have been gathered from [38, 39, 42, 43].

Plate	þ	Solid phase (þ$_\mathrm{s}$)	liquid phase (þ$_\mathrm{l}$)
Steel	κ	$62.8 - 0.039\,T$	—
Steel	c_{v}	$0.5985 - 0.00156\,T + 6.9 \cdot 10^{-6}\,T^2 - 8.221 \cdot 10^{-9}\,T^3 + 2.94 \cdot 10^{-12}\,T^4$	—
Alumin.	κ	$236.4 + 0.054\,T - 2.743 \cdot 10^{-4}T^2 + 1.94 \cdot 10^{-7}\,T^3$	$70.45 + 0.0307\,T$
Alumin.	c_p	$0.88 + 0.00109\,T - 4.54 \cdot 10^{-6}\,T^2 + 1.02 \cdot 10^{-8}T^3 - 7.1 \cdot 10^{-12}T^4$	1.177
Alumin.	μ	$2.47 - 0.00176\,T$	$2.47 - 0.00176\,T$
Back.	κ	$13.5 + 0.015375\,T$	—
Back.	c_{v}	$0.4875 + 0.0001625\,T$	—
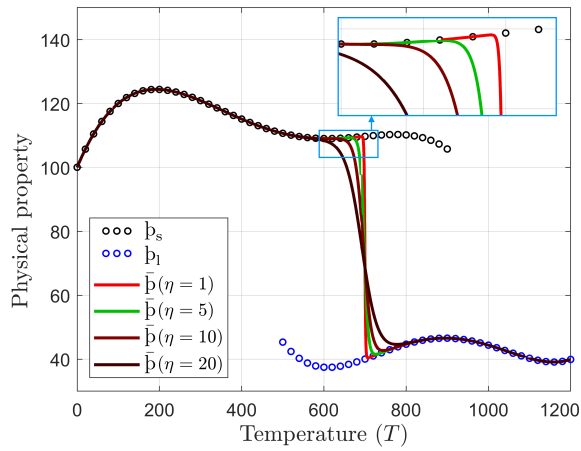
Fig. A1 Smoothing of a physical parameter in the phase change zone. Dots represent polynomial functions that fit and extrapolate some experimental points. The solid lines are the smooth continuous functions ($\bar{\text{þ}}$) that define the physical parameter over the entire temperature range.

physical property in the solid (þ$_\mathrm{s}$) and liquid (þ$_\mathrm{l}$) phase. Function $\bar{\text{þ}}$ considers both phases and smooths the transition for different values of η. In this work, $\eta = 5$ is used, which gives a smoothing over approximately 30 °C with the centre at the melting point (T_{m}), thus $T_{\mathrm{sol}} \approx 660 - 15$ °C and $T_{\mathrm{sol}} \approx 660 + 15$ °C.

References

[1] Kristian Martinsen, Shixin Jack Hu, and Blair E. Carlson. Joining of dissimilar materials. *Cirp Annals*, 64(2):679–699, 2015.

[2] Camille van der Rest, Pascal J Jacques, and Aude Simar. On the joining of steel and aluminium by means of a new friction melt bonding process. *Scripta Materialia*, 77:25–28, 2014.

[3] Tomasz Wegrzyn, J Piwnik, Rafal Burdzik, G Wojnar, and Damian Hadryś. New welding technologies for car body frame welding. *Archives of Materials Science and Engineering*, 58(2):245–249, 2012.

[4] Norberto Jimenez-Mena, Pascal J Jacques, Jean-Marie Drezet, and Aude Simar. On the prediction of hot tearing in Al-to-steel welding by friction melt bonding. *Metallurgical and Materials Transactions A*, 49:2692–2704, 2018.

[5] Stéphane Crucifix, Camille van der Rest, Norberto Jimenez-Mena, Pascal J. Jacques, and Aude Simar. Modelling thermal cycles and intermetallic growth during friction melt bonding of ULC steel to aluminium alloy 2024-T3. *Science and Technology of Welding and Joining*, 20(4):319–324, 2015.

[6] Amin Abdollahzadeh, Behrouz Bagheri, Alireza H Vaneghi, Ali Shamsipur, and Seyyed E Mirsalehi. Advances in simulation and experimental study on intermetallic formation and thermomechanical evolution of Al–Cu composite with Zn interlayer: Effect of spot pass and shoulder diameter during the pinless friction stir spot welding process.

Proceedings of the Institution of Mechanical Engineers, Part L: Journal of Materials: Design and Applications, 237(6):1475–1494, 2023.

[7] David Schmicker, Per-Olof Persson, and Jens Strackeljan. Implicit geometry meshing for the simulation of rotary friction welding. Journal of Computational Physics, 270:478–489, 2014.

[8] Abu Bakar Dawood, Shahid Ikramullah Butt, Ghulam Hussain, Mansoor Ahmed Siddiqui, Adnan Maqsood, and Faping Zhang. Thermal model of rotary friction welding for similar and dissimilar metals. Metals, 7(6):224, 2017.

[9] Xiaocong He, Fengshou Gu, and Andrew Ball. A review of numerical analysis of friction stir welding. Progress in Materials Science, 65:1–66, 2014.

[10] Mostafa Akbari, Parviz Asadi, and Tomasz Sadowski. A review on friction stir welding/processing: Numerical modeling. Materials, 16(17):5890, 2023.

[11] Mingming Tong. Review of particle-based computational methods and their application in the computational modelling of welding, casting and additive manufacturing. Metals, 13(8):1392, 2023.

[12] Mohamadreza Afrasiabi and Markus Bambach. Modelling and simulation of metal additive manufacturing processes with particle methods: A review. Virtual and Physical Prototyping, 18(1):e2274494, 2023.

[13] Sergio R Idelsohn, Eugenio Oñate, and Facundo Del Pin. The particle finite element method: a powerful tool to solve incompressible flows with free-surfaces and breaking waves. International journal for numerical methods in engineering, 61(7):964–989, 2004.

[14] Massimiliano Cremonesi, Alessandro Franci, Sergio Idelsohn, and Eugenio Oñate. A state of the art review of the particle finite element method (PFEM). Archives of Computational Methods in Engineering, 27:1709–1735, 2020.

[15] Alessandro Franci, Massimiliano Cremonesi, Umberto Perego, Giovanni Crosta, and Eugenio Oñate. 3d simulation of vajont disaster. part 1: Numerical formulation and validation. Engineering Geology, 279:105854, 2020.

[16] Alessandro Franci, Eugenio Oñate, Josep Maria Carbonell, and Michele Chiumenti. PFEM formulation for thermo-coupled FSI analysis. application to nuclear core melt accident. Computer Methods in Applied Mechanics and Engineering, 325:711–732, 2017.

[17] Billy-Joe Bobach, Romain Boman, Diego Celentano, Vincent E Terrapon, and Jean-Philippe Ponthot. Simulation of the Marangoni effect and phase change using the particle finite element method. Applied Sciences, 11(24):11893, 2021.

[18] Billy-Joe Bobach, Romain Boman, Josep Maria Carbonell, Luc Papeleux, Eduardo Felipe Fernandez Sanchez, and Jean-Philippe Ponthot. A unified thermo-fluid–solid formulation for FSI and phase change problems based on the particle finite element method. International Journal of Computational Methods, 2024.

[19] Marco-Lucio Cerquaglia, David Thomas, Romain Boman, Vincent Terrapon, and Jean-Philippe Ponthot. A fully partitioned Lagrangian framework for FSI problems characterized by free surfaces, large solid deformations and displacements, and strong added-mass effects. Computer Methods in Applied Mechanics and Engineering, 348:409–442, 2019.

[20] Martin Lacroix, Simon Février, Eduardo Fernández, Luc Papeleux, Romain Boman, and Jean-Philippe Ponthot. A comparative study of interpolation algorithms on non-matching meshes for PFEM-FEM fluid-structure interactions. Computers & Mathematics with Applications, 155:51–65, 2024.

[21] METAFOR: An object-oriented Finite Element code for the simulation of solids submitted to large deformations. http://metafor.

ltas.ulg.ac.be/dokuwiki/. Accessed: 2023-11-30.

[22] Philippe Bussetta, Narges Dialami, Michele Chiumenti, Carlos Agelet de Saracibar, Miguel Cervera, and Jean-Philippe Ponthot. 3D numerical models of FSW processes with non-cylindrical pin. *Advances in Materials and Processing Technologies*, 1(3-4):275–287, 2015.

[23] Simon Février. Travail de fin d'études: Development of a compressible flow solver for PFEM fluid simulations. *Université de Liège, Liège, Belgique*, 2020.

[24] David Thomas, Marco Lucio Cerquaglia, Romain Boman, Thomas D Economon, Juan J Alonso, Grigorios Dimitriadis, and Vincent E Terrapon. CUPyDO-An integrated python environment for coupled fluid-structure simulations. *Advances in Engineering Software*, 128:69–85, 2019.

[25] MG Cooper, BB Mikic, and M Michael Yovanovich. Thermal contact conductance. *International Journal of heat and mass transfer*, 12(3):279–300, 1969.

[26] Roxane Koeune and Jean-Philippe Ponthot. A one phase thermomechanical model for the numerical simulation of semi-solid material behavior. application to thixoforming. *International Journal of Plasticity*, 58:120–153, 2014.

[27] Laurent Adam and Jean-Philippe Ponthot. Thermomechanical modeling of metals at finite strains: First and mixed order finite elements. *International Journal of Solids and Structures*, 42(21-22):5615–5655, 2005.

[28] Gaetan Wautelet and Jean Philippe Ponthot. The influence of equivalent contact area computation in extended node to surface contact elements. *Key Engineering Materials*, 618:1–22, 2014.

[29] Peter S Cook and Anthony B Murphy. Simulation of melt pool behaviour during additive manufacturing: Underlying physics and progress. *Additive Manufacturing*, 31:100909, 2020.

[30] Marco Lucio Cerquaglia. *Development of a fully-partitioned PFEM-FEM approach for fluid-structure interaction problems characterized by free surfaces, large solid deformations, and strong added-mass effects*. PhD thesis, ULiège-Université de Liège, 2019.

[31] Eduardo Fernández, Simon Février, Martin Lacroix, Romain Boman, and Jean-Philippe Ponthot. Generalized-α scheme in the PFEM for velocity-pressure and displacement-pressure formulations of the incompressible Navier–Stokes equations. *International Journal for Numerical Methods in Engineering*, 124(1):40–79, 2023.

[32] Eduardo Fernández, Simon Février, Martin Lacroix, Romain Boman, Luc Papeleux, and Jean-Philippe Ponthot. A particle finite element method based on Level–Set functions. *Journal of Computational Physics*, 487:112187, 2023.

[33] Nicolas Delaissé, Toon Demeester, Dieter Fauconnier, and Joris Degroote. Comparison of different quasi-Newton techniques for coupling of black box solvers. In *14th World Congress on Computational Mechanics/8th European Congress on Computational Methods in Applied Sciences and Engineering*, 2021.

[34] Piotr Organek, Bronisław Gosowski, and Michał Redecki. Relationship between Brinell hardness and the strength of structural steels. In *Structures*, volume 59, page 105701. Elsevier, 2024.

[35] Mary Skidmore and Richard Johnson. Thermal contact conductance of various metals at elevated temperatures. In *24th Thermophysics Conference*, page 1656, 1989.

[36] YF Liu, ZL Hu, DH Shi, and K Yu. Experimental investigation of emissivity of steel. *International Journal of Thermophysics*, 34:496–506, 2013.

[37] Ingrid Martorell, Joan Herrero, and Francesc X Grau. Natural convection from

narrow horizontal plates at moderate rayleigh numbers. *International Journal of heat and mass transfer*, 46(13):2389–2402, 2003.

[38] Panagis Foteinopoulos, Alexios Papacharalampopoulos, and Panagiotis Stavropoulos. On thermal modeling of additive manufacturing processes. *CIRP Journal of Manufacturing Science and Technology*, 20:66–83, 2018.

[39] Matthias Leitner, Thomas Leitner, Alexander Schmon, Kirmanj Aziz, and Gernot Pottlacher. Thermophysical properties of liquid aluminum. *Metallurgical and Materials Transactions A*, 48:3036–3045, 2017.

[40] MO Pekguleryuz, X Li, and CA Aliravci. In-situ investigation of hot tearing in aluminum alloy aa1050 via acoustic emission and cooling curve analysis. *Metallurgical and Materials Transactions A*, 40:1436–1456, 2009.

[41] Norberto Jimenez Mena. *Optimization of the friction melt bonding of aluminium and steel: from microstructure evolution to mechanical properties*. PhD thesis, UCL-Université Catholique de Louvain, 2018.

[42] Cho Yen Ho, Ralph Waterbury Powell, and Peter E Liley. Thermal conductivity of the elements. *Journal of Physical and Chemical Reference Data*, 1(2):279–421, 1972.

[43] Marc J Assael, Konstantinos Kakosimos, R Michael Banish, Jürgen Brillo, Ivan Egry, Robert Brooks, Peter N Quested, Kenneth C Mills, Akira Nagashima, Yuzuru Sato, et al. Reference data for the density and viscosity of liquid aluminum and liquid iron. *Journal of physical and chemical reference data*, 35(1):285–300, 2006.